

The Characterization and Radiative Impact of a Springtime Mixed-Phase Cloudy Boundary Layer observed during SHEBA

P. ZUIDEMA¹, B. BAKER², Y. HAN³, J. INTRIERI⁴, J. KEY⁵, P. LAWSON², S. MATROSOV¹, M. SHUPE⁶, R. STONE⁷, T. UTTAL⁴

¹*Cooperative Institute for Research in Environmental Sciences/NOAA Environmental Technology Laboratory, Boulder, CO*

²*Stratton Park Engineering Company, Boulder, CO*

³*NOAA National Environmental Satellite, Data, and Information Service, Camp Springs, MD*

⁴*NOAA Environmental Technology Laboratory, Boulder, CO*

⁵*NOAA National Environmental Satellite, Data, and Information Service, Madison, WI*

⁶*Science and Technology Corporation/NOAA Environmental Technology Laboratory, Boulder, CO*

⁷*Cooperative Institute for Research in Environmental Sciences/NOAA Climate Monitoring Diagnostics Laboratory, Boulder, CO*

ABSTRACT

The liquid and ice phase water contents, effective particle radii, and volume extinction coefficients of a cloud observed above the Surface Heat Budget of the Arctic experiment site from May 1 - May 10, 1998 are individually retrieved. Cloud radar data (35-GHz) vertically resolves the ice component. A depolarization lidar establishes the base of the liquid cloud while a temperature inversion establishes the liquid cloud top, and an adiabatic ascent calculation applied to a saturated cloud-base parcel establishes the liquid water content profile. The adiabatic calculation is constrained by liquid water paths physically retrieved from microwave radiometer data, for liquid water paths exceeding 15 g m^{-2} . The liquid and ice characterization is aided and validated with aircraft measurements from May 4 and May 7. The cloud radar retrievals of the ice microphysics compare well with aircraft measurements, despite the presence of much larger liquid water contents than ice water contents. Observed and calculated downwelling surface broadband infrared and solar fluxes show good agreement, with biases of 1 and 3 W m^{-2} , respectively, over the May 1 - May 8 time period. The time-mean liquid cloud optical depth of 10.1 ± 7.0 far surpasses the mean ice cloud optical depth of 0.2, so that the radiative (flux) impact of the cloud is close to that of a pure liquid cloud. Two mechanisms are observed by which ice regulates the overall cloud optical depth: sedimentation from an upper ice cloud, and a local ice production mechanism with a timescale of a few hours, thought to reflect a preferred freezing of the larger liquid drops. Although both mechanisms uptake liquid water, it is of equal interest that the liquid water paths replenish quickly, within a half-day or less, attesting to strong water vapor fluxes. Longer-time-scale variations in cloud optical depth synchronize with the depth of the cloudy boundary layer. The radiative impact of the cloud upon the surface is significant: a time-mean net cloud forcing of 41 W m^{-2} with a diurnal amplitude of $\sim 20 \text{ W m}^{-2}$. This is primarily a consequence of a high surface reflectance (0.86). For the low-optical-depth cloudy columns, the net cloud forcing is sensitive to cloud optical depth, while for the high-optical-depth cloudy columns, the important sensitivity is to the surface reflectance. Because clouds were almost always present, and almost 60% of the cloudy columns had optical depths > 6 , any future increase in the springtime cloud optical depth at this location (76°N , 165°W) may not significantly alter the surface radiation budget.

Corresponding author address:

P. Zuidema, NOAA/ETL/ET6 325 Broadway, Boulder, CO

80305 (paquita.zuidema@noaa.gov)

1. Introduction

Recent indications of Arctic climate change include a rapid warming of the Arctic surface (Chen et al. 2002; Serreze et al. 2000; Stone 1997), decreasing sea-ice extent and thickness (Chapman and Walsh 1993; Parkinson et al. 1999), changes in water vapor advection (Groves and Francis 2002) and vegetation changes (Sturm et al. 2001). Coincident with these surface and hydrological changes, Wang and Key (2003) show increased spring and summer cloudiness and decreased winter cloudiness using satellite data spanning 1982-1999. Surface observations at Barrow, Alaska also report an increasing spring cloudiness (Stone et al. 2002), and an increasing cloud optical depth (Dutton et al. 2003).

Other studies emphasize the radiative importance of clouds to the Arctic surface (Curry and Ebert 1992; Intrieri et al. 2002a; Schweiger and Key 1994; Walsh and Chapman 1998). A modeling study concludes that during springtime, a persistent cloud cover can advance the snowmelt onset date by up to one month from that of clear-sky conditions (Zhang et al. 1996). Given recent Arctic climate changes, an improved understanding of Arctic cloud optical properties is required for the elucidation of cloud-radiation-surface feedbacks, particularly for transition-season clouds.

Arctic clouds are often mixed-phase¹, as the liquid phase is common even in sub-freezing conditions. Liquid was observed 73% of the time in depolarization lidar data during the year-long Surface Heat Budget of the Arctic (SHEBA) experiment (Intrieri et al. 2002b; Uttal and co authors 2002). Both phases of mixed-phase clouds are radiatively important. Super-cooled liquid contributes prominently to the overall cloud optical depth (Hogan et al. 2002; Sun and Shine 1994) and increases the measured surface infrared flux, especially during the Arctic winter months (Intrieri et al. 2002a). The ice phase is often less optically significant, but is important for indirectly regulating the overall cloud optical depth. When present, ice is quick to uptake water vapor and water; this transition can be associated with a large drop in cloud optical depth (Curry and Ebert 1992; Sun and Shine 1994). Mixed-phase cloud longevity is sensitive to even modest ice particle and ice freezing nuclei concentrations (Harrington et al. 1999; Jiang et al. 2000; Morrison et al. 2003; Pinto 1998), so that the inclusion of mixed-phase microphysics is necessary for the simulation of the annual cycle in Arctic cloudiness (Vavrus 2003).

Despite the increased attention to the Arctic climate

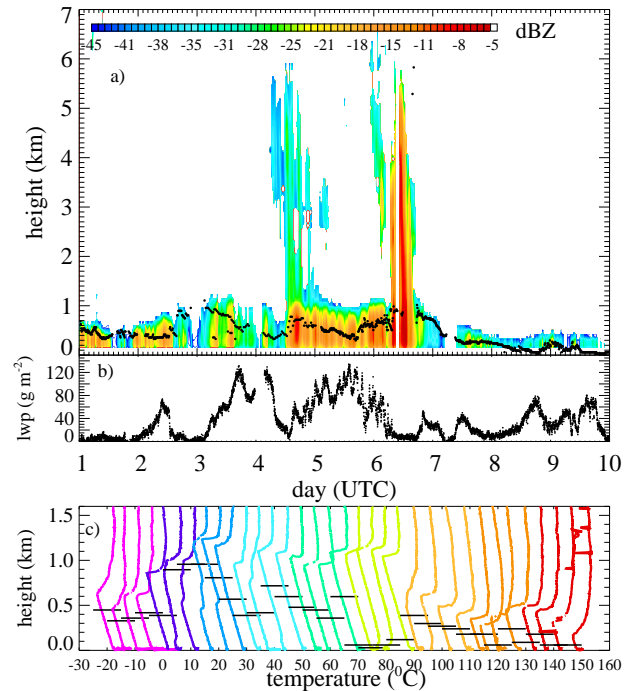


FIG. 1. a) May 1 - May 10 radar reflectivities in dBZ, with black dots indicating the lidar-determined water cloud bases, b) microwave radiometer-derived liquid water path, and c) all the temperature soundings. Each temperature sounding is displaced by 5 °C from the previous sounding, with each day represented by a different color. The lines across the temperature profiles indicate the lidar-determined cloud base.

¹A mixed-phase cloud is defined loosely here as liquid and ice co-existing near each other, usually within the same vertical column.

over the past decade, the ability to separately characterize the liquid and ice cloud component has remained elusive. Most remote sensors and retrieval methods are designed for only the liquid or ice phase. Methods for simultaneous retrieval utilizing radar/lidar combinations (Hogan et al. 2002), near-infrared spectra (Daniel et al. 2002) and infrared spectra (Turner et al. 2003) have been proposed; these are best suited for clouds of low optical depth and do not necessarily provide vertically-resolved profiles.

The study presented here utilizes a conventional approach that lacks these limitations. The focus is on a long-lasting, surface-based, mixed-layer, mixed-phase cloud occurring from May 1 - May 10, 1998 at the SHEBA site, approximately 3 weeks prior to the snowmelt onset date. Retrievals from multiple surface remote sensor measurements (35-GHz cloud radar, depolarization lidar, microwave radiometer) are combined with rawinsonde temperature measurements to individually characterize the ice and liquid components. The presence of only one liquid layer during our time period of interest eases the determination of the liquid and ice vertical structure. The cloud radar measurements vertically resolve the ice phase component. The depolarization lidar establishes the base of the liquid cloud, a temperature inversion identifies the liquid cloud top, and an adiabatic ascent calculation applied to a parcel saturated at cloud base establishes the liquid water content profile. Liquid water paths (LWPs) derived from a surface-based microwave radiometer constrain the adiabatically-derived LWPs for LWPs $> 15 \text{ g m}^{-2}$.

A multi-sensor/adiabatic characterization has been used previously. Examples include Stankov et al. (1995), who examined winter continental icing conditions, and Albrecht et al. (1990), who compared remotely-sensed liquid water paths against adiabatic ascent calculations for stratus clouds. The approach may be particularly useful for Arctic mixed-phase clouds, as liquid in the Arctic environment is often adiabatically-distributed (Curry 1986; Curry et al. 1988, 1996; Herman and Curry 1984; Hobbs and Rangno 1998; Jayaweera and Ohtake 1973; Lawson et al. 2001; Pinto et al. 2001; Shupe et al. 2001). Temperature soundings can aid cloud-top identification because longwave radiational cooling will strengthen a cloud-top temperature inversion if present. For the case examined here, comparisons to aircraft data aid and validate the characterization, as does a comparison of modeled to observed radiative fluxes at the surface.

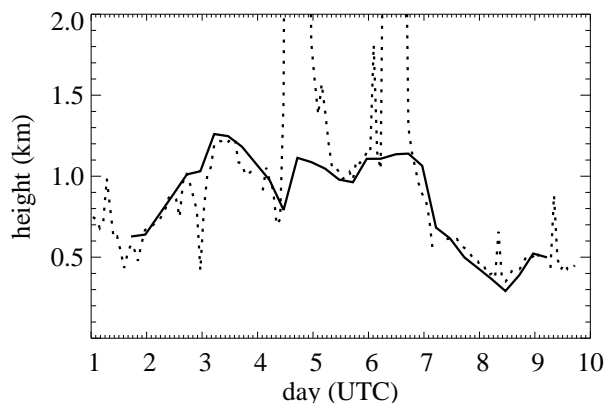


FIG. 2. Radar-determined cloud top (dashed line) and inversion height (solid line) for the May 1 - May 10 time period.

2. Case Description and Data

a. Surface Instrumentation and Data Description

Table 1 lists the primary surface-based remote sensors utilized within this study; all are vertically-pointing but the sunphotometer, which tracks with the Sun. The 35-GHz cloud radar retrieval of the ice component is described more fully in Section 4a. The cloud radar has a beamwidth of 0.5° beam width, and a sensitivity of -46 dBZ at 5 km without attenuation. The water cloud bases are established with the Depolarization and Backscatter Unattended Lidar (Intrieri et al. 2002b). Low lidar depolarization ratios (usually < 0.11) indicate sphericity, either from liquid drops or hydrated aerosols. A large change in the lidar backscattered intensity further delineates the base of a water cloud.

Liquid water paths are physically retrieved from the microwave radiometer (MWR) brightness temperatures (Y. Han, unpublished data). The physical retrieval uses the dry opacity and cloud liquid absorption models of Rosenkranz (1998) and Liebe et al. (1991), consistent with the recommendations of Westwater et al. (2001). The cloud liquid absorption values for temperatures below 0°C are less certain, as they are extrapolations of values from warmer temperatures. In addition, the retrieval utilizes an estimated temperature for the liquid cloud. The liquid cloud temperatures are estimated from the soundings, the lidar-determined liquid cloud base and an assumed cloud thickness of 400 m. The use of a liquid cloud temperature reduces the retrieval error to 10 g m^{-2} . This is a valuable improvement on the statistical retrieval error of 25 g m^{-2} (Westwater et al. 2001) for

Table 1: Surface-based instrumentation

| Instrument | Vertical Res. | Primary Application | Reference |
|---|---------------|----------------------------|-------------------------|
| 35 GHz cloud radar | 45 m | retrieval of ice component | Moran et al. (1998) |
| 23.8 and 31.8 GHz microwave radiometer | integrated | liquid water path | Westwater et al. (2001) |
| 0.5235 μm polarized micropulse lidar | 30 m | cloud phase | Alvarez et al. (1998) |
| Rawinsondes (4 times per day) | | pressure, temperature | |
| Sunphotometer (500 and 675 nm) | integrated | aerosol optical depth | Stone et al. (1993) |

Table 2: Aircraft instrumentation

| Instrument | Parameter | Range |
|---------------------------|--|----------------------------------|
| FSSP ¹ -100 | cloud drop and crystal size distribution | 2-47 μm particle size |
| 1D OAP ² -260X | drop and crystal size distribution | 40-640 μm |
| Cloud Particle Imager | cloud particle phase, shape, and size | 5-2000 μm |
| King Hot-wire probe | liquid water content | 0.05-3.0 g m^{-3} |

¹Forward Scattering Spectrometer Probe²Optical Array Probe

the low liquid water paths common to the Arctic². Liquid water paths are retrieved at a 2 minute time resolution.

b. Aircraft Data Description

Table 2 lists the aircraft instrumentation used within this study. We utilized data from the first and second FIRE/ACE research flights of the NCAR C-130 aircraft, occurring on May 4 and May 7 respectively. Liquid water contents (LWCs) were determined by the mean of the two King hot-wire probes³. The King liquid water contents were initially increased by a factor of 1.2, based upon analysis results by K. Laursen at NCAR⁴ of the King probe sensor surface area. The FSSP-100 data establish the dropsize effective radius, and the logarithm of the geometric standard deviation (hereafter referred to as lognormal width) of the droplet distribution.

The FSSP probe consistently overestimated LWC during the FIRE/ACE project (Lawson et al. 2001), and is more prone to overestimates in drop sizing than to counting errors. We applied a correction to the FSSP data to achieve consistency with the King probe liquid water contents. The FSSP bin sizes were reduced by raising them to a fractional power a , where a is the ratio between the mean King probe LWC and the FSSP LWC. This effectively reduces the drop sizes, particularly of the largest drops, while preserving the bin concentrations and not allowing the lowest bin to go below 0 μm . Separate values of a were calculated for individual time periods.

²The statistical retrieval utilizes a mean climatological sounding from Barrow, Alaska, and no information on the liquid cloud altitude or temperature.

³One King probe was present on the left side of the airplane, and another on the right side. Their values were typically within 10% of each other.

⁴National Center of Atmospheric Research

Statistically meaningful values can be derived from the aircraft liquid water data at high time resolution. In contrast, Cloud Particle Imager (CPI) data on ice microphysics are collected at a slower rate, and approximately one-minute time segments were necessary towards constructing a representative size distribution. These correspond to a horizontal distance from the SHEBA site of 4-5 km or less. Complete size distribution spanning from 2 to 2000 microns were estimated from combining the FSSP, CPI, and 260X data. The CPI size distribution is self-scaled, on the assumption that the concentration of the larger particles ($\sim 250 \mu\text{m}$) can be accurately calculated (Lawson 2003); the CPI size distributions agreed well with the FSSP size distribution in regions of overlap. The 260X probe undercounts particles (Lawson 2003), and in regions where the CPI and 260X size distributions overlapped, the CPI values were preferentially chosen.

After a complete size distribution was estimated, the size distributions were divided into their ice and liquid components. The King probe served as the primary indicator of liquid. The FSSP data were assumed to correspond completely to liquid particles when liquid was present, and the CPI data were partitioned by phase using a roundness criterion. Although the FSSP-100 probe was probably also given to sizing problems within all-ice conditions, no correction was then applied because of a lack of additional information. In liquid-containing regions, the adiabatic shape of the FSSP LWC profile supports the assumption that the FSSP probe senses little ice.

c. Case Description

By early May, the SHEBA ice camp had drifted to approximately 76°N, 165°W. An anticyclone existed to its northwest during late April to mid-May (Curry and

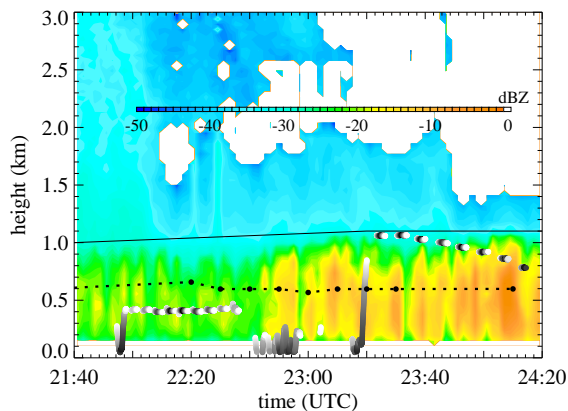


FIG. 3. May 4 aircraft overflights of the SHEBA site projected upon the radar reflectivities. The horizontal distance between the shown aircraft overflights and the SHEBA site are all within ten km, with the smaller horizontal distances shown in darker shades. The lidar-determined water cloud base is shown as a dotted black line and the temperature inversion as a solid line.

co authors 2000), inducing large-scale subsidence to its southeast. Throughout May 1 - May 10, a low, super-cooled liquid cloud persisted within a surface-based mixed-layer, and upper ice clouds are apparent within the cloud radar measurements on May 4 and May 6. After May 7, the low cloud slowly thinned, consistent with increased subsidence reported for that day (Wylie and Hudson 2002). The low cloud dissipated completely at solar noon on May 9, but developed again later and lasted until mid-May. Two leads, several meters wide, opened near the SHEBA ship around May 7 (Curry and co authors 2000). Aspects of the May 1 - May 10 time period are discussed in Curry and co authors (2000) and Lawson et al. (2001), and form the subject of at least two model simulations (Carrió et al. 2003; Morrison et al. 2003).

The cloud radar reflectivities, lidar-determined water cloud bases, microwave radiometer-derived liquid water paths, and all the temperature soundings from May 1 - May 10 are shown in Fig. 1. The lidar, microwave radiometer, and radiosonde measurements indicate the lower cloud contained super-cooled liquid (temperature $\approx -21^\circ\text{C}$) while high radar reflectivity values, Doppler velocities, and high radar spectral width⁵ values indicate

⁵The spectral width is defined as the square root of the variance of sampled Doppler velocities about their mean value. High values can indicate turbulence, but in the Arctic, where turbulence is low, often indicate a wide distribution of Doppler velocities associated with the presence of two phases. On May 4, regions determined by the aircraft to contain both phases also corresponded to high values for the radar

the lower cloud also contained ice (see also Fig. 1 of Intrieri et al. (2002b)). The upper clouds are most probably all-ice, based on high values for the radar Doppler velocities, and low values for the radar spectral width.

The radar-reflectivity-determined cloud top usually agreed well with the location of a 2-3 K temperature inversion present during the entire May 1 - May 10 time period (Figure 2). This temperature inversion persisted during times with low liquid water paths (May 6, 7, and 8) and coincided with the liquid cloud top even when the cloud radar data did not clearly distinguish separate low and upper clouds (e.g., May 4, as shown on Fig. 3). The near-surface temperature averaged approximately -18°C during this time period, with a small warming trend (see also Wylie (2001)).

The May 4 aircraft flight path near the SHEBA site, shown projected upon the cloud radar reflectivities in Fig. 3, coincided with the end of sedimentation from an upper cloud into the lower cloud. We compared liquid water data from one aircraft descent (at 21:54 UTC) and ascent (at 23:20 UTC) to adiabatic calculations. The aircraft ice microphysical data come from six horizontal overpasses occurring after 23:20 UTC and a combination of the overpasses occurring between 22:00 and 22:30 UTC. While the later overpasses occurred within mixed-phase conditions, the earlier overpasses were below the liquid cloud in all-ice conditions.

Mixed-phase conditions were still present on May 7, but the cloud had thinned, with MWR-derived liquid water paths falling below their stated error of $\pm 10 \text{ g m}^{-2}$ during the time of the aircraft overflight. We compared liquid water data from three aircraft ascents and descents to the adiabatic parcel calculation, without correcting to the MWR-derived LWP values.

3. Liquid Phase

A liquid water content profile is determined from the adiabatic ascent of an air parcel just saturated at the lidar-determined cloud base and lifted upwards, using the temperature structure interpolated from the nearest-in-time soundings. As the cloud parcel is lifted into colder temperatures, liquid water is condensed. At the warmer cloud-top temperature inversion, the cloudy parcel is no longer able to condense water. The vertically-integrated LWC is then constrained using the MWR-derived liquid water path when the MWR LWP exceeds 15 g m^{-2} (arbitrarily chosen to be 1.5 times the stated error). All the individual temperature soundings show a simple decrease with height until the inversion (Fig. 1c), however,

spectral width.

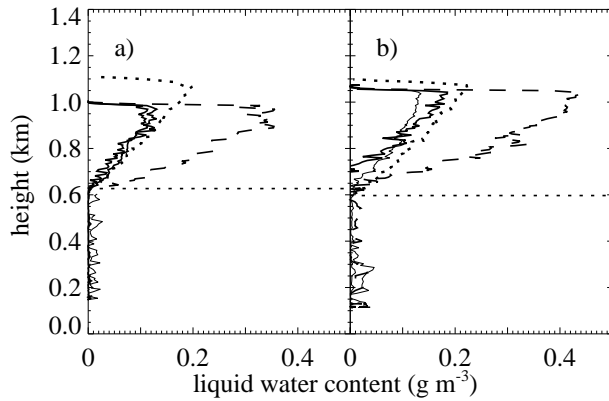


FIG. 4. Aircraft King-probe LWC (thick solid line), uncorrected and corrected FSSP-derived LWCs (dashed and thin solid line), and LWCs calculated from an adiabatic ascent (dotted line) during the May 4 a) 21:53-21:55 descent, and b) 23:18-23:21 ascent. The lidar-determined cloud base is indicated by a thin dotted horizontal line.

the linear-in-time sonde interpolation can generate a double temperature inversion at some times that foster two (false) relative maxima in the liquid water content distribution. In addition, the sonde resolution is initially degraded to match the cloud radar resolution of 45 m, which may introduce some error into the cloud base temperature.

Once a liquid water content profile has been established, the effective radius (r_e) and the volume extinction coefficient (β) are determined. Their derivation utilizes the mean aircraft-determined cloud droplet number concentration (\bar{N}) and assumes a lognormal cloud droplet size distribution with a mean aircraft-determined lognormal width $\overline{\sigma_{\log}}$.

a. Liquid Water Content

Figure 4 shows the adiabatically-determined liquid water content profiles for the May 4 ascent and descent, along with the mean King hot-wire and FSSP LWCs. The aircraft was close to the SHEBA site at the bottom of the cloud bases, and approximately 20 km (descent) or 12 km (ascent) away at the liquid cloud top height. The lidar-determined cloud base of 600 m coincided very well with the aircraft-sensed base. The microwave radiometer-determined liquid water paths are close to the calculated adiabatic maximum for both vertical profiles (95% and 103%).

The constrained adiabatically-calculated LWCs slightly exceed the aircraft LWC values in Figure 4, but the LWCs, vertically integrated to the aircraft-determined

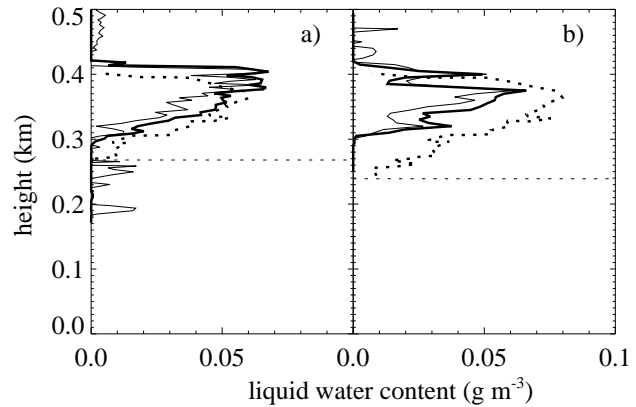


FIG. 5. Corrected FSSP-probe and King-probe LWCs (thick and thin solid lines) and the adiabatic LWC (dotted line) during the May 7 a) 22:16-22:19 descent, and b) 23:07-23:30 overflights binned by altitude. The lidar-determined cloud base is indicated by a horizontal dotted line.

cloud top, agree with the MWR LWP retrieval to within its uncertainty. A high degree of correspondence between the aircraft and calculated LWCs exists, even over regions separated by 5-20 km. This suggests a horizontally homogeneous liquid layer, with variations in LWP mostly related to variations in the height of the temperature inversion. During other flight segments occurring at constant altitude, the aircraft measurements of LWCs varied by less than 25% of their mean values.

The MWR detected negligible liquid water during the May 7 research flight. For this case, the lidar depolarization ratios were low from cloud base to the surface. No liquid precipitation was observed by the aircraft. A more likely cause was aerosols, as observed ice nuclei concentrations reached a maximum of 1645/L, perhaps released from a nearby lead (Rogers et al. 2001). A distinct lidar backscattered intensity gradient (though weaker than that of May 4) still allowed an objective placement of a water cloud base. The lidar-determined liquid cloud base was at or below the aircraft-sensed liquid cloud base for all three vertical profiles, by 0, 30, and 60 m.

For all three profiles, the temperature inversion coincided to within 20 m of the aircraft-sensed cloud top. Two of the three profiles are shown in Figure 5, and indicate the aircraft LWCs are close to their adiabatic maximum values. The adiabatically-derived LWPs can exceed the aircraft-determined LWPs by up to a factor of two, primarily by the lower placement of the liquid cloud base by the lidar than the aircraft. Nevertheless, the lidar-radiosonde-adiabatic combination correctly detected and distributed liquid in a low-LWP situation where the microwave radiometer LWP retrieval was highly uncertain.

b. Determination of N and σ_{log}

Mean values of N and σ_{log} were determined from the corrected FSSP dropsize distributions of the five vertical profiles. Only FSSP number concentration values exceeding 50 cm^{-3} were used, reflecting a screening for ice particles (results were not sensitive to the threshold value). We find a time-mean N of 222, with a standard deviation, using the means of each individual time period, of 14. N varies little with height during any of the five vertical profiles. Observed number concentrations were high relative to the overall FIRE/ACE time period, coinciding with a polluted layer overlying the cloud (Yum and Hudson 2001).

The lognormal width of the distribution can be derived from the observable parameters as

$$\sigma_{log} = \left[\frac{-1}{3} \ln \left(\frac{6LWC}{\pi \rho_w N D_e^3} \right) \right]^{0.5} \quad (1)$$

(Miles et al. 2000) where ρ_w is the density of water and D_e is the effective particle diameter. All values come from the corrected FSSP dropsize distributions. A mean value of $\overline{\sigma_{log}} = 0.242 \pm 0.015$ was determined, and a slight spectral narrowing with height is evident for all 5 vertical profiles⁶.

c. Liquid effective radius and volume extinction coefficient

The moments of the lognormal droplet size distribution are modeled as

$$\langle r^k \rangle = r_o^k \exp \left(\frac{k^2 \sigma_{log}^2}{2} \right) \quad (2)$$

following the notation of Frisch et al. (1995). The effective radius r_e is then

$$r_e = r_o \exp \left(\frac{5\sigma_{log}^2}{2} \right) \quad (3)$$

In terms of the observables LWC, \overline{N} , and $\overline{\sigma_{log}}$,

$$r_e = \left[\frac{3LWC}{4\pi \rho_w \overline{N}} \right]^{\frac{1}{3}} \exp(\overline{\sigma_{log}}^2) [1000] \quad (4)$$

where LWC and ρ_w are in g m^{-3} , \overline{N} in cm^{-3} , and r_e in microns, and

$$\beta = 2\pi \overline{N} r_e^2 \exp(-3\overline{\sigma_{log}}^2) [0.001] \quad (5)$$

with β in km^{-1} .

⁶This is consistent with traditional theory of condensational droplet growth for an adiabatic parcel experiencing no mixing or gravitational collection and was also observed during the Atlantic Stratocumulus Transition Experiment (Gerber 1996), but is counter to most other observations (Miles et al. 2000).

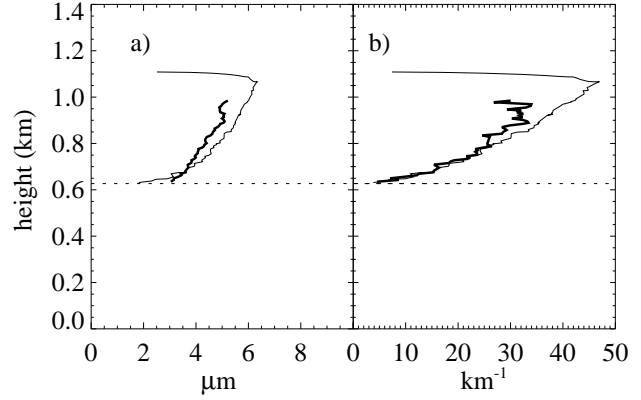


FIG. 6. Comparisons during the May 4 21:53-21:55 descent between the aircraft (thick line) and adiabatically-derived (thin line; $\overline{N}=222$ and $\overline{\sigma_{log}}=0.242$) a) effective particle radius and b) volume extinction coefficient.

An example comparison between the adiabatically-derived and aircraft r_e and β for the May 4 descent is shown in Fig. 6. Fig. 7 shows a comparison for all of the vertical profiles between the liquid optical depths (τ) derived from the aircraft data and from the adiabatic retrieval (with $\overline{N}=222 \text{ cm}^{-3}$ and $\overline{\sigma_{log}}=0.242$). For the May 4 time periods when the MWR-derived LWP constrained the adiabatic calculation, the agreement is to within 10%. For the May 7 time periods, when no MWR-derived LWP measure was used, the agreement is worse, with the adiabatic estimates exceeding the aircraft-derived estimates by up to a factor of 2. This primarily reflects a lower cloud base placement by the lidar than the aircraft. Further low-LWP cases would need to be examined to determine if this is typical.

d. May 1 - May 10 liquid phase time series

Liquid β and r_e , derived using Eqns. (4) and (5), are shown for the May 1 - May 10 time period at a 10-minute resolution in Figure 8, along with the optical depth and layer-averaged effective radius. The mean cloud optical depth is 10.1 ± 7.8 , corresponding to a mean liquid water path of 37 g m^{-2} . The layer-mean effective radius is $4.4 \pm 1.1 \mu\text{m}$, the time-mean cloud top effective radius is $5.4 \pm 1.5 \mu\text{m}$ (this value is most consistent with the time-mean LWP and optical depth), and the LWC-weighted effective radius is $4.8 \pm 1.3 \mu\text{m}$. Cloud optical depth maxima of approximately 30 are apparent on May 3 and May 5, times when no upper cloud was detected and the boundary layer was deeper.

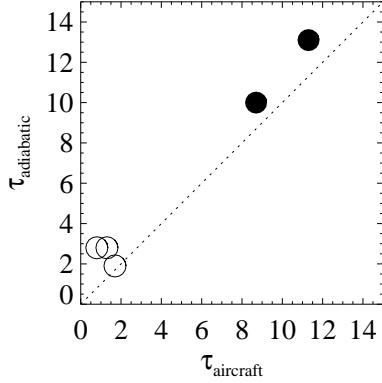


FIG. 7. Cloud optical depth determined adiabatically versus from aircraft corrected FSSP drosize distributions for May 4 (filled circles) and May 7 (open circles).

4. Ice Phase

In contrast to the liquid phase, the retrieval of the ice component depends only on one instrument, the 35-GHz cloud radar. Comparisons between radar and aircraft-determined mean microphysical values are more uncertain for ice than for liquid, however. The cloud radar retrievals are plagued by insensitivity to the smaller particles and to the particle habit (for cloud radars lacking polarization). Particle habit also introduces uncertainty into the treatment of the aircraft data. Additionally, for the aircraft data, the complete size distributions require a compilation of data from three or four instruments sensing different size ranges.

For the purposes of this study we estimate an effective ice particle size $D_{e,i}$ as the ratio of the size distribution volume, at bulk density, to the projected area (Boudala et al. 2002; Matrosov et al. 2003; Mitchell 2002), or,

$$D_{e,i} = 1.5 \frac{IWC}{\rho_i A_p} \quad (6)$$

where ρ_i is the solid ice density of 0.917 g m^{-3} , and A_p is the projected particle area. This definition is useful because it preserves the quantities important for radiative transfer: the total mass is important for the absorption, and the total cross-sectional area is important for the extinction (e.g., Fu 1996).

In practice, we first estimate IWC and β_i , assume an extinction efficiency of two, and calculate $D_{e,i}$ from

$$D_{e,i} = 3 \frac{IWC}{\rho_i \beta_i} \quad (7)$$

By first performing an independent estimate of the volume extinction coefficient and then deriving the particle

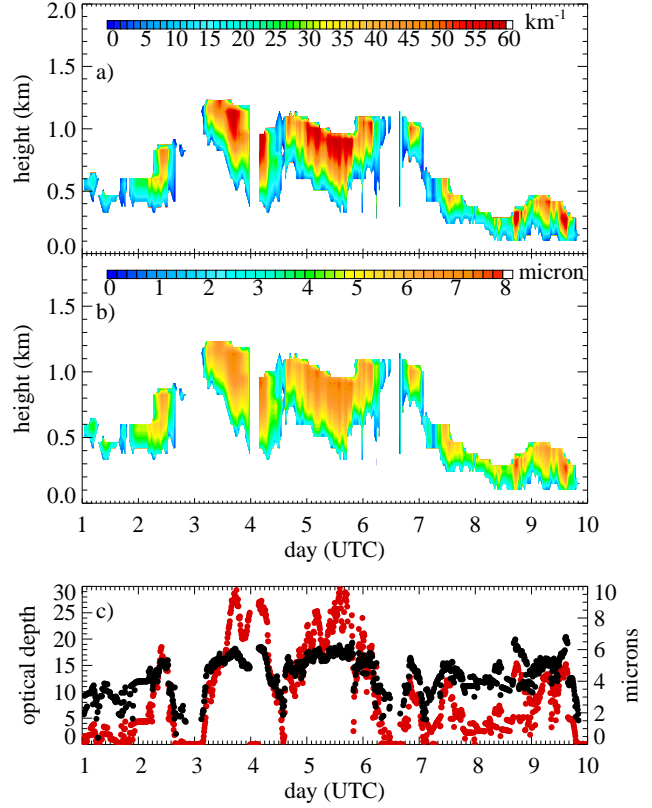


FIG. 8. The retrieved liquid a) volume extinction coefficient, b) effective radius, and c) optical depth (red) and layer-mean effective radius (black).

size estimate from it, the particle size estimate cannot impact the optical depth estimate. This has the advantage that poor particle size estimates are less radiatively influential, as only the associated phase function and single-scattering albedo estimates are affected.

a. Radar Method

A radar-based cloud retrieval technique developed for all-ice clouds is presented in Matrosov et al. (2002, 2003). These studies suggest the retrieval can be extended to retrieve the ice component within mixed-phase conditions, using the assumption that the radar is predominantly sensitive to the larger ice particles. This radar-only technique relies solely on radar reflectivity (Z_e) and the Doppler velocity (V_z). D_o , the median volume size, is estimated from a quadratic fit to V_z (see Matrosov et al. (2002)). The ice water content is calculated as

$$IWC = \frac{Z_e}{GD_o^3} \quad (8)$$

where the coefficient G assumes an exponential particle size distribution and the following individual ice particle bulk density-size relationship for individual particle sizes D greater than 0.1 mm (Brown and Francis 1995; Locatelli and Hobbs 1974):

$$\rho \approx 0.07D^{-1.1} \quad (9)$$

where ρ is given in g cm^{-3} .

The volume extinction coefficient is estimated as

$$\beta_i = \frac{Z_e}{XD_o^4} \quad (10)$$

where the coefficient X depends on the same assumptions as the coefficient G and additionally on a mass-area-size relationship estimated in c-g-s units as

$$\frac{m}{A_p} = 0.038D^{0.576} \quad (11)$$

(A. Heymsfield, pers. comm.; see Heymsfield et al. (2002)), where m is the individual particle mass.

A correction $V_z(h) = BV_z(h_0)$ is initially applied to account for the variation of dry air density with height:

$$B = \exp\left(\frac{z}{z_{sh}}\right)^{2.5 \times 10^{-3} V_z + 0.1} \quad (12)$$

for $V_z < 100 \text{ cm s}^{-1}$, and

$$B = \exp\left(\frac{z}{z_{sh}}\right)^{0.35} \quad (13)$$

for $V_z > 100 \text{ cm s}^{-1}$, with z in km, V_z in cm s^{-1} and z_{sh} referring to a scale height of 8.5 km. A running 20-minute average of the radar reflectivity and Doppler velocity data is initially created from one-minute data to diminish the influence of larger-scale vertical air motion. The IWC and β_i retrieval uncertainties are estimated by a factor of two.

b. Radar-Aircraft Comparison

A feature of the CPI data is that the individual particle area and perimeter are known. This information, in addition to particle length and width, improves estimates of IWC (Baker et al. 2002; Boudala et al. 2002). A reflectivity and IWC calculation that assumes the Brown-Francis density-size relationship is also done, to allow comparison to the retrieval method of Matrosov et al. (2002). The FSSP data were left uncorrected for this comparison, so that the values for the liquid component represent a conservative overestimate.

Figure 9 shows comparisons for May 4 between radar-derived and aircraft-derived values for a) radar reflectivity, b) ice and liquid water content, c) extinction coefficient, and d) effective ice particle size. The aircraft data come from the horizontal overpasses depicted in Fig. 3 and described in Section 2d. The comparisons within the mixed-phase region are more robust lower in the cloud, where ice concentrations were higher. In contrast to the homogeneity of the liquid water field, the ice hydrometeor field can be highly variable, as indicated by the standard deviations of the cloud radar reflectivity values about a 20-minute mean (Fig. 9a). The mean reflectivity values, measured and calculated from aircraft data, are similar, confirming that the liquid component contributed negligibly to the radar reflectivity (and independently confirmed by low reflectivities calculated from the FSSP data alone). Although the reflectivity comparison suggests that the Brown and Francis (1995) density-size relationship is appropriate, the 260X probe is thought to undercount particle number (Lawson 2003), and the good agreement may reflect a compensation of errors.

Figure 9c shows that the radar-retrieved ice water contents are slightly higher than the aircraft values, but they agree to within the uncertainty of the retrieval (estimated as a factor of 2). At the upper part of the cloud, much of the contribution to the IWC comes from large, complex particle shapes, reflecting sedimentation from upper ice clouds. At these low IWC values or large particle sizes, the Baker et al. (2002) method appears to agree better with the radar-retrieved IWC values than the method using the Brown and Francis (1995) density-size relationship. The aircraft overestimate of the low reflectivity val-

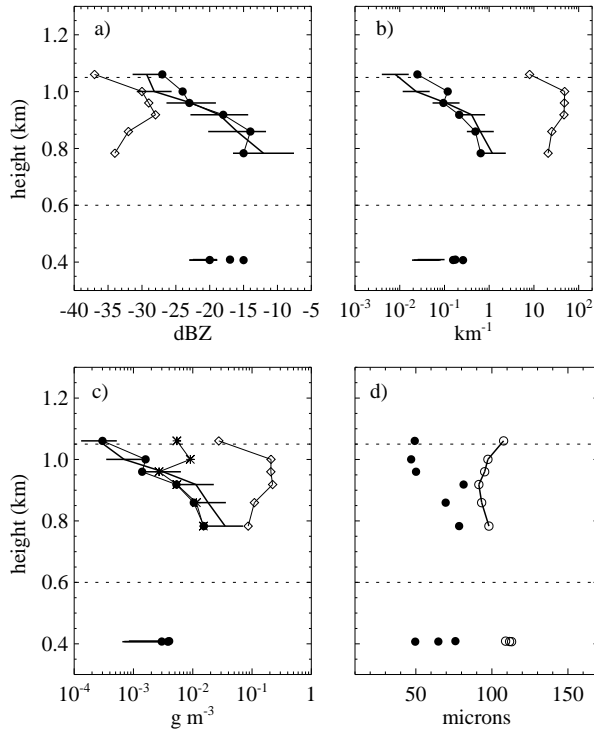


FIG. 9. Comparisons for the May 4 aircraft overflights of the cloud radar between the radar-derived ice microphysics (black line with error bars) and aircraft-derived microphysical values for liquid and ice (filled diamonds and circles) of a) reflectivity, b) volume extinction coefficient, c) liquid and ice water content, and d) effective ice particle size (open circles denote the radar values). Two different methods for calculating ice water contents from the aircraft data are shown: the asterisks assume the Brown and Francis (1995) particle density-size relationship, while the filled circles follow the Baker et al. (2002) method. Dotted lines indicate the liquid cloud boundaries.

ues shown in Fig. 9a may support this, as it is similarly computed assuming the Brown-Francis density relationship.

The radar retrievals of β_i are slightly higher than the aircraft values within lower regions of the cloud, while the radar-retrieved effective particle sizes exceed the aircraft effective particle sizes by factors between one to two. Since the effective particle size is derived from the ratio of IWC/β_i , this means the radar IWC estimate exceeds the aircraft IWC estimate proportionally more, than the radar β_i estimate exceeds the aircraft β_i .

In summary, despite the uncertainties in both the radar and the aircraft estimates, two robust conclusions can be made from Figure 9. One is that the total cloud optical depth is dominated by the liquid component (Fig. 9b). The second is that the radar retrievals of IWC and β_i (Fig. 9b and c) agree with the aircraft-determined values to within the retrieval uncertainty, even at liquid and ice water contents of 0.2 and 0.001 g m⁻³ respectively. This supports the suggestion of Matrosov et al. (2002, 2003) that radar-only retrievals originally designed for all-ice clouds can be extended to mixed-phase conditions.

c. May 1 - May 10 ice phase time series

The time series of the radar-retrieved ice β_i and effective radius, and total ice optical depth and layer-averaged ice particle radius are shown in Figure 10. The effective radius is shown rather than the effective diameter to aid comparison to Fig. 8. The mean ice cloud optical depth is 0.236, with occasional values of 2 to 6. The layer-mean effective radius is 49 ± 7 μ m, close to the mean IWC -weighted effective radius of 46. Increased values for β_i are evident within the lower cloud at times when upper clouds are present.

d. Radiative Impact of the Ice

Two mechanisms by which ice can diminish LWP and thereby the cloud optical depth are evident in Fig. 11, which shows a time series of the ice water contents and liquid water paths. The first is upper ice cloud sedimentation into the liquid-bearing cloud occurring on May 4 and May 6. These are associated with a near-complete and complete depletion of the LWP. The second mechanism, apparent on May 5 in particular, is a local variability in IWC associated with smaller changes in LWP, occurring on a time scale of a few hours.

The mechanism for the locally-produced IWC has been suggested by Morrison et al. (2003), and involves a cycle wherein liquid droplets above a diameter threshold of approximately 20 μ m freeze preferentially, grow, and

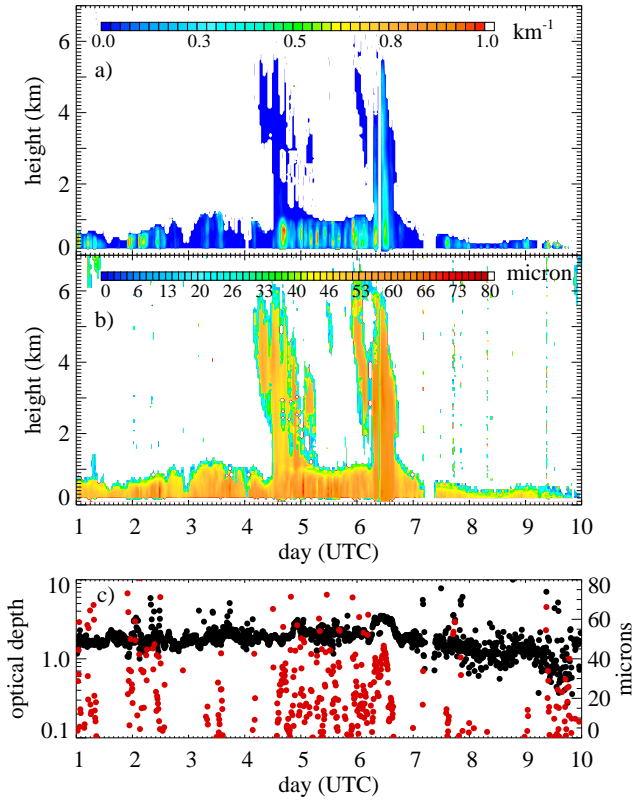


FIG. 10. Radar-retrieved ice a) volume extinction coefficients, b) effective ice particle radius, and c) total ice cloud optical depth (red) and mean effective ice particle radius (black), from May 1 - May 10.

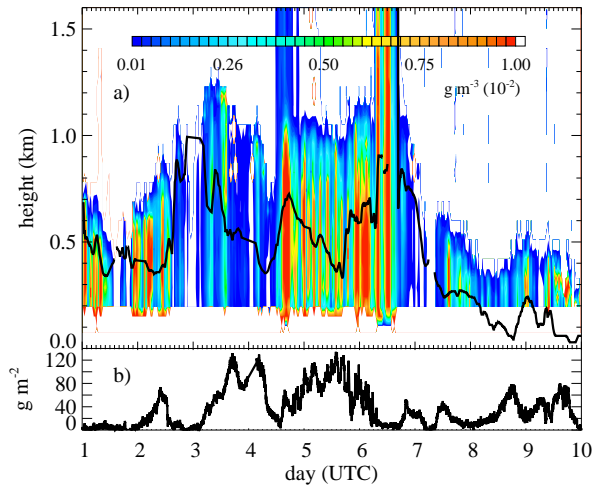


FIG. 11. a) Radar-retrieved ice water contents from May 1 to May 10, with the lidar-determined liquid cloud base (black line) and b) microwave-radiometer-determined liquid water paths.

rapidly accrete (Hobbs and Rangno 1985; Korolev et al. 2003; Rangno and Hobbs 2001). Thereafter, new ice particles are not produced again until coalescence-collision builds up a population of large drops. Only a small population of large drops exceeding a threshold diameter are necessary (Hobbs and Rangno 1985); their existence, despite the high N measurements and narrow droplet distribution width, is supported by the values shown in Fig. 8. For example, on May 5, cloud-top effective diameters of over $16 \mu\text{m}$ are retrieved. Drizzle droplets were also observed by the May 4 aircraft research flight after 2300 UTC (Lawson et al. 2001). The mechanism should be - and often is observed to be - more active during times when the boundary layer is deeper and the liquid water paths are higher, creating more opportunities for the formation of large liquid cloud drops.

An interesting counter-example is also apparent, with little ice production occurring on May 3 and the beginning of May 4, despite a relatively deep boundary layer, high LWP, and cloud-top effective radii similar to that of May 5. One modifier of the cyclical ice production may be intermittent entrainment of the overlying polluted layer (Carrió et al. 2003). The contact nucleation mechanism of Hobbs and Rangno (1985) proposes that particular aerosol particle types (“contact nuclei”) come into contact with supercooled liquid drops and cause them to freeze at a higher temperature than they would through other modes of nucleation. Variable contact nuclei concentrations within the overlying air, along with varying entrainment, may help explain differences between May 3 and May 5 ice production.

It is also evident in Fig. 11 that the liquid is quickly replenished after each depletion by ice, attesting to strong water vapor fluxes, either local or through large-scale advection. A longer-time-scale variability in the cloud optical depth is related to the boundary layer deepening and shallowing over time (see, e.g., Fig. 1). This may reflect temporal changes in the large-scale descent rate (e.g., Wylie and Hudson 2002), so that ultimately the large-scale subsidence rate may be the primary factor influencing the cloud optical depth.

5. Sensitivity analysis for the liquid volume extinction coefficient

The much larger liquid cloud optical depth means that the radiative (flux) impact of the cloud is close to that of a pure liquid cloud. We rely strongly on the adiabatic assumption for the liquid’s characterization. This is because cloud radar measurements applied within all-liquid cloud conditions to derive mean liquid cloud microphysical values (Frisch et al. 1995, 1998, 2002; Shupe

et al. 2001) and the liquid volume extinction coefficient (Zuidema and Evans 1998), cannot be used in mixed-phase (or light drizzle) conditions. A sensitivity analysis demonstrates that an adiabatic characterization of β is also more robust than a cloud radar-based estimate lacking additional information on N , as the adiabatic calculation is less sensitive to variability in N and σ_{log} .

The adiabatically-derived β is given by

$$\beta = 1.65(\pi N)^{1/3} \left(\frac{LWC}{\rho_w} \right)^{2/3} \exp(-\sigma_{log}^2) \quad (14)$$

through combining Eqn. (5) with Eqn. (4). The sensitivity of β to N , σ_{log} , and LWC is

$$\frac{\partial \ln \beta}{\partial \ln N} = \frac{1}{3} \quad (15)$$

$$\frac{\partial \ln \beta}{\partial \ln \sigma_{log}} = -2\sigma_{log}^2 \quad (16)$$

$$\frac{\partial \ln \beta}{\partial \ln LWC} = \frac{2}{3} \quad (17)$$

For a retrieval of β based upon cloud radar data and an assumed number concentration,

$$\beta = \frac{\pi}{2} \exp(-4\sigma_{log}^2) Z^{1/3} N^{2/3} \quad (18)$$

(Frisch et al. 1995). Excluding the radar reflectivity, the sensitivity of β is only on N and σ_{log} :

$$\frac{\partial \ln \beta}{\partial \ln N} = \frac{2}{3} \quad (19)$$

$$\frac{\partial \ln \beta}{\partial \ln \sigma_{log}} = -8\sigma_{log}^2 \quad (20)$$

The latter cloud-radar based derivation of β is four times more sensitive to variations in σ_{log} and twice as sensitive to variations in N , than an adiabatic characterization.

Eqns. 15-20 assume that N is not known. If a microwave radiometer is available along with the cloud radar, a number concentration can be derived and implemented within the cloud radar retrieval. In that case, the sensitivities of the cloud radar/radiometer technique are similar to those for the adiabatic characterization. Both approaches will have a similar sensitivity to the LWC uncertainty, although the source of the uncertainty will be different (microwave radiometer versus some assumed fraction of the adiabatic maximum). For the low LWP cases common to the Arctic, a purely adiabatic characterization is also sensitive to how well the cloud boundaries are known (as demonstrated for May 7 in Fig. 7).

6. Radiative Flux Closure and Cloud Forcing

A comparison of the observed and modeled radiative fluxes at the surface over the May 1 - May 8 time period further encourages confidence in the data and the retrievals. The calculated net cloud forcing demonstrates that the clouds provided a net warming of the surface, aiding sea-ice melt and advancing the onset date of snowmelt (from that of clear-sky conditions). Sensitivity tests elucidate the radiative impact of uncertainty in the LWPs and surface reflectances, as well as their importance within climate change scenarios.

a. Data and Method

Radiative fluxes were calculated with the medium-band (24 shortwave and 105 longwave bands, the latter at 20 cm^{-1} resolution) radiative transfer model Streamer (Key 2001). The cloud radiation uses a discrete ordinates code (DISORT version 2; Stamnes et al. 2000) with 48 streams. A strength of the model is its comprehensiveness and adaptation for the Arctic climate. For example, the model allows for the representation of two separate phases within a single volume, and shortwave ice cloud optical property parameterizations for seven different ice particle habits are available (Key et al. 2002). The model shortwave spectral resolution should adequately represent the observed spectral variation of surface albedo. A model weakness with impact for the radiative flux comparison is that only 4 gases are considered (H_2O , O_3 , CO_2 , and O_2) and the gaseous line information database is outdated (LOWTRANS 3B Selby et al. 1976). We modified Streamer to incorporate Mie phase functions (for the liquid phase) and the radar data.

Objective examination of the CPI imagery determined that on May 4 and May 7 most of the contribution to the total ice mass and area came from irregular aggregates, including some rimed aggregates. This is consistent with a more comprehensive analysis of Arctic ice cloud properties (Korolev et al. 1999).

SHEBA spectral surface albedo data (Perovich et al. 2002) were averaged and extrapolated to match the Streamer spectral resolution, and interpolated in time to a daily resolution. A time-mean broadband albedo of 0.86 typified the dry-snow-covered icescape, with a standard deviation of almost zero. This mean broadband albedo matches the mean albedo calculated from the surface radiation fluxes measured at the Atmospheric Surface Flux Group (ASFG) tower. The ASFG albedos are more variable, however, and have a standard deviation of 0.05. The observed fluxes have a downwelling shortwave flux uncertainty of $\pm 3\%$ with a bias of -5 to $+1 \text{ W m}^{-2}$, and a downwelling longwave flux uncertainty of $\pm 2.5 \text{ W m}^{-2}$.

(Persson et al. 2002).

Arctic haze aerosol vertical profiles, available within Streamer, were constrained using total aerosol optical depth data derived from sunphotometer measurements (R. Stone, unpublished data). In late April the total aerosol optical depth increased sharply, and thereafter slowly diminished with time. Clear-sky measurements made on April 25 (all day) and May 7 (5:30-8:30 UTC) correspond to total aerosol optical depths interpolated to $0.6 \mu\text{m}$ of 0.144 and 0.124, respectively, using an Ångström exponent derived from the optical depths at 675 and $500 \mu\text{m}$. Column ozone amounts from the Total Ozone Monitoring Satellite were used to scale the McClatchey Arctic vertical ozone profile; 393 Dobson units were measured on May 18 and 24 (J. Pinto, pers. comm.).

Initially, clear-sky conditions were modeled to evaluate the aerosol specification. Hourly-averaged May 7 modeled and observed shortwave and infrared fluxes agree to within 1 W m^{-2} . May 7 was also modeled using the higher aerosol optical depth value from April 25, and this decreased the modeled surface shortwave radiative fluxes by 2 W m^{-2} . On the basis of these comparisons, a time-mean aerosol optical depth of 0.135 (at $0.6 \mu\text{m}$) was used for the May 1 - May 10 time period. Deviations from this value not exceeding the sunphotometer observations for April 25 and May 7 can only account for a variation of 2 W m^{-2} in the downward shortwave flux.

b. Comparison

The comparison between the modeled and observed broadband downwelling infrared and shortwave surface fluxes is shown in Figure 12. Over the May 1 - May 8 time period, the modeled downwelling surface longwave fluxes exceeded the observed surface longwave fluxes by 1 W m^{-2} , with a root-mean-square (RMS) deviation of 13 W m^{-2} , or 7% of the observed values. The modeled downwelling surface shortwave fluxes exceeded the observed fluxes by 3 W m^{-2} (1% of the observed fluxes), with an RMS deviation of 17 W m^{-2} , or 12% of observed fluxes. The small bias encourages confidence in the data, although complete agreement cannot be achieved without exceeding estimated uncertainties in LWP and the surface reflectance (Section 6d). The bias is slightly larger for low liquid water path time periods (2 and 3.5 W m^{-2} for the longwave and shortwave comparisons, respectively). Although this indicates the value of incorporating the microwave-radiometer-derived LWPs, the small bias again demonstrates that the cloud was close to its adiabatic maximum throughout this time period.

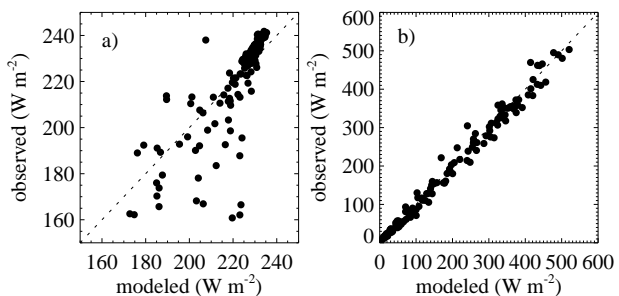


FIG. 12. Modeled and observed broadband downwelling surface a) infrared fluxes and b) shortwave fluxes, from May 1 through May 7. (May 8 and 9 were excluded because the observed fluxes were suspect, containing a diurnal cycle offset of approximately 1 hour from the modeled fluxes). Only cloudy values are shown.

c. Cloud Forcing

By early May the Sun was at or above the horizon, with a mean and noon-time solar zenith angle of approximately 74° and 60° , respectively. The all-sky downwelling shortwave fluxes were decreased significantly by the persistent cloud presence, a time-mean decrease of 55 W m^{-2} relative to clear-sky conditions. This exceeded the increase in downwelling longwave fluxes of 49 W m^{-2} compared to clear skies. Nevertheless, because of the high surface albedo, the shortwave cloud forcing⁷ averaged only -12 W m^{-2} , whereas the time-mean longwave cloud forcing was 53 W m^{-2} . The time-mean net cloud forcing of 41 W m^{-2} was modulated by a diurnal amplitude of approximately 20 W m^{-2} . For some days (May 2, 7, and 9), a diurnal cycle in the cloud optical depth was observed that is also typical for lower-latitude stratus, with a nighttime maximum and cloud thinning during and after solar noon (Wood et al. 2002; Zuidema and Hartmann 1995). Such a cloud diurnal cycle further minimizes the diurnal-mean shortwave cloud forcing.

The net cloud surface forcing is shown as a function of cloud optical depth in Figure 13. Approximately 30% of the cloud optical depths were less than 3, and almost 60% were greater than 6. For cloud optical depths less

⁷The net cloud forcing is the sum of the longwave and shortwave cloud forcing, where each separate cloud forcing is the difference between the net surface flux with the cloud, and without the cloud (as calculated from Streamer). The net surface flux is the difference between the downwelling and upwelling fluxes, where both are positive quantities. A positive cloud forcing represents a warming of the surface.

than 3, the net cloud forcing is dominated by the longwave component, and is highly sensitive to optical depth. For cloud optical depths greater than 6, the longwave cloud forcing is relatively independent of cloud optical depth, and instead the net cloud forcing is modulated by the shortwave component. This modulation is at best one-half of the mean net cloud forcing, varying mostly with solar zenith angle and cloud optical depth, given a near-constant surface reflectance. Changes in the surface reflectance will alter this modulation.

d. Sensitivity of cloud forcing to surface reflectance and liquid water path

A satellite-based study of Antarctic cloud radiative forcing concludes that cloud forcing is most sensitive to changes in cloud amount, surface reflectance, cloud optical depth, and cloud-top pressure (Pavolonis and Key 2003). For the case examined here, cloud amount is almost constantly high and the cloud top pressure is well-determined by the 4X-daily soundings. The LWP values have uncertainties of $\pm 10 \text{ g m}^{-2}$, however, and the surface reflectance values contain potential uncertainties. A sensitivity assessment can also provide insight into how the net cloud forcing of the surface may change within a future climate change scenario, for example, to a boundary-layer deepening that is reflected in higher LWPs.

For the sensitivity to LWP changes, all MWR-derived LWPs were altered by ± 5 and $\pm 20 \text{ g m}^{-2}$. These serve as an upper bound on the impact of random uncertainty and uncertain biases from, for example, over- or under-estimated cloud liquid absorption values for below-freezing conditions. For this sensitivity analysis all adiabatically-calculated LWPs were corrected to the MWR-derived LWP, regardless of the actual MWR-derived LWP value (i.e., no threshold of 15 g m^{-2} was applied). A reference calculation was also done with the MWR-derived LWP values applied irrespective of their values. This led to a decrease to 23% of cloudy columns with optical depths $< 3 \%$.

Changes in the longwave and shortwave cloud forcing compensated each other for much of the LWP change. An increase in the LWP of 5 and 20 g m^{-2} led to an increased net cloud forcing of 2 and 3 W m^{-2} . The small sensitivity is remarkable, given a reference \overline{LWP} of 37 g m^{-2} , and occurs because most cloudy columns are already optically thick so that the radiative impact is insensitive to further increases. A decrease in the LWP of 5 and 20 g m^{-2} leads to a decrease in the net cloud forcing of -3.5 and -10 W m^{-2} , respectively. This sensitivity is much stronger because more cloudy columns become

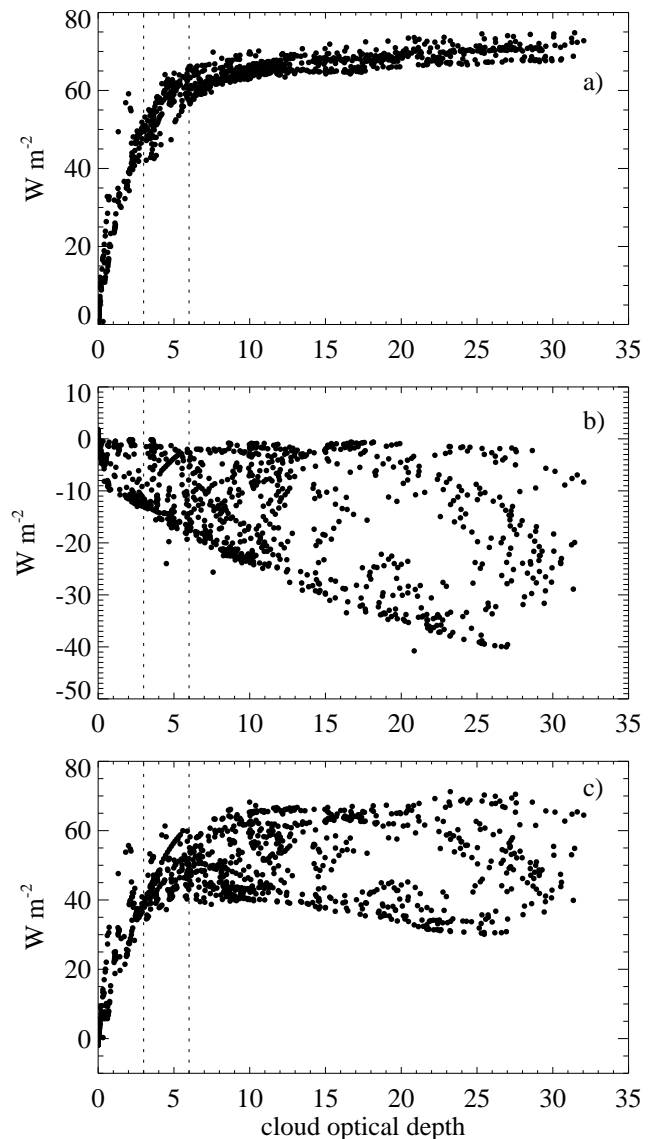


FIG. 13. a) Longwave, b) shortwave, and c) net cloud surface forcing as a function of cloud optical depth. Dotted lines denote optical depths of 3 and 6.

optically thin. Future climate change scenarios are more likely to include increases than decreases in springtime optical depths; the LWP sensitivity assessment suggests that at this location, where the majority of the cloudy columns exceed optical depths of 6, the radiative impact upon the surface may be insignificant.

Uncertainties in the surface reflectance arise from spatial and temporal sampling limitations, and natural variability arising from overhead cloudiness preferentially reflecting/absorbing certain wavelengths, and solar zenith angle changes. A change in the surface reflectance of -0.05 and $+0.05$ changed both the mean shortwave and net cloud forcing by -3.8 W m^{-2} and $+4.5 \text{ W m}^{-2}$, respectively. Much more dramatic surface reflectance changes can plausibly occur within future climate change scenarios, so that surface reflectance changes may have an important radiative impact.

e. Net Radiative Heating Rates

Ignoring the interruptions introduced by the upper-level clouds, the long-lived colloidal stability of this case contrasts with a previous study that finds quick depletion of liquid with ice nuclei concentrations of 4/L and a cloud top of -13°C (Harrington et al. 1999). Mean observed ice nuclei concentrations were 18/L, reaching maxima of 73/L on May 4 and even 1645/L on May 7 (see Table 2; Rogers et al. 2001). The observed longevity may attest to strong water vapor fluxes (either local or large-scale advection) and also to strong cloud-top radiative cooling rates. As discussed in Pinto (1998), at cooling rates exceeding 50 K/day , cloud lifetimes will exceed a day regardless of the ice nuclei concentrations. From May 4 through May 6, cloud-top cooling rates exceeded 65 K/day (not shown). These high cooling rates generate enough turbulence to promote mixing down to the surface, facilitating surface sensible and latent heat fluxes that also help maintain the cloud layer (Wang et al. 2001). This helps explain the observation of Curry and co authors (2000), that surface-based mixed layers are thought uncommon in the Arctic, but that their occurrence is most likely in May when the surface is warming rapidly. On May 7 and thereafter, the cloud-top cooling rates diminished to 35 K/day . These, along with strong subsidence rates (Wylie and Hudson 2002) and the entrainment of the overlying warm, dry air, will contribute to the observed cloud thinning. A diurnal cycle in the cloud-top cooling is more evident after May 7, with solar warming offsetting the longwave cooling near solar noon (approximately 23–24 UTC), further aiding dissipation (not shown).

7. Summary and Discussion

Arctic mixed-phase clouds are common, challenging to characterize, and important to the radiative forcing of the Arctic surface. Surface-based remote sensors can characterize clouds with greater confidence than is practical with current satellite instruments, and provide a larger-scale context to aircraft data analyses. In the study presented here, we have undertaken an analysis of a mixed-phase cloud existing from May 1 until May 10 at the SHEBA site. A 35-GHz cloud radar vertically resolves the ice component. The liquid cloud base is identified through a low lidar depolarization ratio, a temperature inversion indicates the cloud top, and the MWR-derived liquid water path constrains an adiabatic parcel calculation of the liquid water content. The MWR-derived LWPs use a physical retrieval that incorporates the liquid cloud temperature, reducing the retrieved LWP uncertainty to 10 g m^{-2} . This is a valuable improvement over the statistical retrieval error of 25 g m^{-2} for the typically low-liquid-water Arctic clouds.

Aircraft observations from 2 vertical profiles on May 4, and 3 profiles on May 7, establish the liquid cloud droplet number concentrations and droplet distribution widths, for a time-mean N of 222 cm^{-3} and time-mean σ_{log} of 0.242. A homogeneity was observed within the liquid water field, with similar values for N and σ_{log} on May 4 and 7, and little horizontal-scale LWC variability for May 4. The \overline{N} and $\overline{\sigma_{log}}$ help determine the liquid effective radius and volume extinction coefficient. An adiabatic characterization, when applicable, is particularly useful for mixed-phase or (lightly) drizzling situations where cloud radar measurements cannot identify the cloud liquid component. A sensitivity analysis also demonstrates that an adiabatically-derived β is less sensitive to variability and uncertainty in N , σ_{log} , and liquid water content, than a β derived from cloud radar data, in all-liquid situations where both techniques can be applied and no microwave radiometer measurements are available.

A comparison is done between the aircraft and radar-retrieved ice mean microphysical values. In contrast to the liquid water field, the ice hydrometeor field is highly inhomogeneous. Despite the presence of much larger liquid water contents than ice water contents, the ice component is responsible for almost all of the (radar) reflectivity. This supports the suggestion of Matrosov et al. (2002, 2003) that radar-only retrievals originally designed for all-ice clouds can be extended to mixed-phase conditions. The radar and aircraft estimates of ice water content and volume extinction coefficient agree to within the radar retrieval uncertainty (estimated as a fac-

tor of two). The effective particle size is determined from the ratio of the estimated IWC to β_i ; the independent estimate of β_i means that uncertainty in the particle size estimate only impacts the single-scattering albedo and phase function or asymmetry parameter. The radar retrievals accurately capture the vertical variation of the ice component. Calculations of the ice water content using the method of Baker et al. (2002) may perform better (judged by the comparison to the radar retrievals at low IWC values) than IWCs calculated using the Brown and Francis density relationship.

The mean liquid optical depth is approximately 10 with maxima of 30, and the mean ice cloud optical depth is 0.2 with maxima of 2 to 6. The much larger liquid cloud optical depth means that the radiative (flux) impact of the cloud is close to that of a pure liquid cloud. Observed and calculated downwelling surface broadband infrared and solar fluxes agree to within 1 and 3 W m^{-2} , respectively, over a May 1 - May 8 time period. Both biases are within 1% of the observed fluxes. The longwave and shortwave RMS deviations are, respectively, 13 and 17 W m^{-2} , or 7% and 12% of observed fluxes.

Previous studies have highlighted the sensitivity of mixed-phase cloud longevity to modest ice freezing nuclei concentrations (Harrington et al. 1999; Jiang et al. 2000; Pinto 1998). In the study presented here, two mechanisms were observed by which ice affected the cloud liquid water content and optical depth. One mechanism is the sedimentation of ice particles from an upper cloud on May 4 and May 6, leading to near depletion of the liquid and large decreases in cloud optical depth. The other is a local ice production mechanism with a time scale of a few hours; it is particularly pronounced for May 5 (Fig. 11). One plausible explanation for the locally-generated ice particle population is a preferred freezing of liquid droplets exceeding a diameter threshold of approximately 20 μm (Hobbs and Rangno 1985; Morrison et al. 2003; Rangno and Hobbs 2001).

Although both mechanisms uptake liquid water and decrease the cloud optical depth, it is of equal interest that the liquid water paths replenish quickly despite the cold ($\sim -20^\circ\text{C}$) conditions, within a half-day or less after the passage of an upper ice cloud, or within a few hours for the local ice production. Longer-time-scale changes in the cloud optical depth synchronize with changes in boundary layer depth, which in turn may reflect variability in the large-scale subsidence (Wylie and Hudson 2002). The almost-constant liquid presence attests to strong water vapor fluxes, either through large-scale advection or local processes. Locally, strong cloud-top radiative cooling rates ($> 50 \text{ K/day}$) help maintain the mixed-phase cloudy boundary layer despite high mean

ice nuclei measurements relative to those used within modeling studies (e.g., Harrington et al. 1999), by promoting boundary-layer-depth mixing and thereby surface latent heat fluxes.

The radiative impact of the cloud upon the surface is significant: a time-mean net cloud forcing of 41 W m^{-2} , modulated by a diurnal amplitude of $\sim 20 \text{ W m}^{-2}$. The consistently positive net cloud forcing is primarily a consequence of the high surface albedo (mean value of 0.86), as downwelling shortwave surface fluxes are decreased more by the presence of the cloud, than the downwelling infrared surface fluxes are increased (by the cloud presence). Approximately 30% of the cloud optical depths are < 3 , and almost 60% are > 6 . For the low-optical-depth cloudy columns, the net cloud forcing is highly sensitive to cloud optical depth. For the high-optical-depth cloudy columns, the important sensitivity is to the surface reflectance.

Recent observations indicate increasing springtime Arctic cloudiness (Stone et al. 2002; Wang and Key 2003) and possibly in cloud optical depth (Dutton et al. 2003). For the case presented here, the cloudiness amount is already high, and a more plausible future climate scenario is an increase in the springtime cloud optical depth. Such an increase may not significantly alter the surface radiation budget at this location (76°N , 165°W), because the majority of the cloudy columns are already optically thick. Otherwise, the net cloud forcing of the surface may be most affected by future climate change scenarios invoking changes in the surface reflectance.

Acknowledgments. The first author was supported throughout most of this study by a National Research Council Research Associateship Award. The contribution of Robert Stone and Taneil Uttal was supported through the NOAA Studies of Environmental Arctic Change (SEARCH) program. Jeffrey Key's participation was supported through the NOAA SEARCH program and NSF grant OPP-0240827. Support from NSF SHEBA (agreement #OPP-9701730 and OPP-0084257) for the collection and processing of data from the cloud radar, microwave radiometer, and depolarization lidar is gratefully acknowledged. Graham Feingold introduced us to the sensitivity analysis notation used in Section 5. Streamer is publicly available through the website <http://stratus.ssec.wisc.edu/streamer/>.

REFERENCES

- Albrecht, B. A., C. Fairall, D. Thomson, A. White, and J. Snider, 1990: Surface-based remote sensing of the observed and the adiabatic liquid water content. *Geophys. Res. Lett.*, **17**, 89–92.

- Alvarez, R., W. Eberhard, J. Intrieri, C. Grund, and S. Sandberg, 1998: A depolarization and backscatter lidar for unattended operation in varied meteorological conditions. *10th AMS Symp. on Met. Obs. Instr.*, pp. Jan. 11–16 Phoenix, AZ.
- Baker, B., C. Schmitt, P. Lawson, and D. Mitchell, 2002: Further analysis and improvements of ice crystal mass-size relationships. *11th AMS Conference on Cloud Physics*, pp. 3–7 June, Ogden, UT.
- Boudala, F., G. Isaac, Q. Fu, and S. Cober, 2002: Parameterization of effective ice particle size for high-latitude clouds. *Int. J. Climatol.*, **22**, 1267–1284.
- Brown, P. R. A., and P. N. Francis, 1995: Improved measurements of the ice water content in cirrus using a total-water probe. *J. Atmos. Oceanic. Tech.*, **12**, 410–414.
- Carrió, G. G., H. Jiang, and W. R. Cotton, 2003: Impact of aerosol intrusions on the Arctic boundary layer and on sea-ice melting rates Part I: May 4, 1998 case. *J. Atmos. Sci.*. Submitted.
- Chapman, W. L., and J. E. Walsh, 1993: Recent variations of sea ice and air temperatures in high latitudes. *Bull. Am. Meteorol. Soc.*, **73**, 33–47.
- Chen, Y., J. A. Francis, and J. R. Miller, 2002: Surface temperature of the Arctic: Comparison of TOVS satellite retrievals with surface observations. *J. Clim.*, **15**, 3698–3708.
- Curry, J. A., 1986: Interactions among turbulence, radiation and microphysics in Arctic stratus clouds. *J. Atmos. Sci.*, **43**, 90–106.
- Curry, J. A., and co authors, 2000: FIRE Arctic Clouds Experiment. *Bull. Amer. Meteorol. Soc.*, **81**, 5–29.
- Curry, J. A., and E. E. Ebert, 1992: Annual cycle of radiative fluxes over the Arctic Ocean: Sensitivity to cloud optical properties. *J. Climate*, **5**, 1267–1280.
- Curry, J. A., E. E. Ebert, and G. F. Herman, 1988: Mean and turbulence structure of the summertime Arctic cloudy boundary layer. *Q. J. R. Meteorol. Soc.*, **114**, 715–746.
- Curry, J. A., W. B. Rossow, D. Randall, and J. L. Schramm, 1996: Overview of Arctic cloud and radiation characteristics. *J. Climate*, **9**, 1731–1764.
- Daniel, J. S., S. Solomon, R. Portmann, A. O. Langford, and C. S. Eubank, 2002: Cloud liquid water and ice measurements from spectrally resolved near-infrared observations: A new technique. *J. Geophys. Res.*, **107**, doi:10.1029/2001JD000,688.
- Dutton, E., A. Farhadi, R. Stone, C. Long, and D. Nelson, 2003: Long-term variations in the occurrence and effective solar transmission of clouds as determined from surface-based irradiance observations. *J. Geophys. Res.*, p. submitted.
- Frisch, A. S., C. W. Fairall, and J. B. Snider, 1995: Measurement of stratus cloud and drizzle parameters in ASTEX with a K_{α} -band Doppler radar and a microwave radiometer. *J. Atmos. Sci.*, **52**, 2788–2799.
- Frisch, A. S., G. Feingold, C. W. Fairall, T. Uttal, and J. B. Snider, 1998: On cloud radar and microwave radiometer measurements of stratus cloud liquid water profiles. *J. Geophys. Res.*, **103**, 23,195–23,197.
- Frisch, A. S., M. Shupe, I. Djalalova, G. Feingold, and M. Poellot, 2002: The retrieval of stratus cloud droplet effective radius with cloud radars. *J. Atmos. Oc. Tech.*, **19**, 835–842.
- Fu, Q., 1996: An accurate parameterization of the solar radiative properties of cirrus clouds for climate models. *J. Climate*, **9**, 2058–2082.
- Gerber, H., 1996: Microphysics of marine stratocumulus clouds with two drizzle modes. *J. Atmos. Sci.*, **53**, 1363–1377.
- Groves, D. G., and J. A. Francis, 2002: Variability of the Arctic atmospheric moisture budget from TOVS satellite data. *J. Geophys. Res.*, **107**, doi:10.1029/2002JD002,285.
- Harrington, J. Y., T. Reisin, W. R. Cotton, and S. M. Kreidenweis, 1999: Cloud resolving simulations of Arctic stratus. part II: Transition-season clouds. *Atmos. Res.*, **51**, 45–75.
- Herman, G. F., and J. A. Curry, 1984: Observational and theoretical studies of solar radiation in Arctic stratus clouds. *J. Clim. Appl. Meteor.*, **23**, 5–24.
- Heymsfield, A. J., A. Bansemar, S. Lewis, J. Iaquinta, M. Kajikawa, C. Twohy, and M. Poellot, 2002: A general approach for deriving the properties of cirrus and stratiform ice cloud particles. *J. Atmos. Sci.*, **59**, 3–29.
- Hobbs, P. V., and A. L. Rangno, 1985: Ice particle concentrations in clouds. *J. Atmos. Sci.*, **42**, 2523–2549.
- Hobbs, P. V., and A. L. Rangno, 1998: Microstructures of low and middle-level clouds over the Beaufort Sea. *Quart. J. Roy. Meteor. Soc.*, **124**, 2035–2071.
- Hogan, R., P. Francis, H. Flentje, A. Illingworth, M. Quante, and J. Pelon, 2002: Characteristics of mixed-phase clouds part I: Lidar, radar and aircraft observations from CLARE '98. *Q. J. R. Meteorol. Soc.*, **128**, 28 pp.
- Intrieri, J., C. Fairall, M. Shupe, P. Persson, E. Andreas, P. Guest, and R. Moritz, 2002a: An annual cycle of Arctic surface cloud forcing at SHEBA. *J. Geophys. Res.*, **107**, (C10) 10.1029/2000JC000,439.
- Intrieri, J., M. Shupe, T. Uttal, and B. McCarty, 2002b: An annual cycle of Arctic cloud characteristics observed by radar and lidar at SHEBA. *J. Geophys. Res.*, **107**, (C10) 10.1029/2000JC000,423.
- Jayaweera, K., and T. Ohtake, 1973: Concentration of ice crystals in arctic stratus clouds. *J. Res. Atmos.*, **7**, 199–207.
- Jiang, H., W. R. Cotton, J. O. Pinto, J. A. Curry, and M. J. Weissbluth, 2000: Cloud resolving simulations of mixed-phase arctic stratus observed during BASE: Sensitivity to concentration of ice crystals and large-scale heat and moisture advection. *J. Atmos. Sci.*, **57**, 2105–2117.
- Key, J., 2001: Streamer user's guide. *Cooperative Institute for Meteorological Satellite Studies*, p. 96 pp.
- Key, J., P. Yang, B. Baum, and S. Nasiri, 2002: Parameterization of shortwave ice cloud optical properties for various particle habits. *J. Geophys. Res.*, **107**, 742–752.
- Korolev, A., G. A. Isaac, and J. Hallett, 1999: Ice particle habits in Arctic clouds. *Geophys. Res. Lett.*, **26**, 1299–1302.
- Korolev, A., G. A. Isaac, S. G. Cober, J. W. Strapp, and J. Hallett, 2003: Microphysical characterization of mixed-phase clouds. *Quart. J. Roy. Met. Soc.*, **129**, 39–65.

- Lawson, R., 2003: Continued quality-control and analysis of aircraft microphysical measurements. *Final Report*, pp. NASA FIRE.ACE LaRC PO No. L-14,363.
- Lawson, R., B. A. Baker, C. G. Schmitt, and T. L. Jensen, 2001: An overview of microphysical properties of Arctic clouds observed in May and July 1998 during FIRE ACE. *J. Geophys. Res.*, **106**, 14,989–15,014.
- Liebe, H. J., G. A. Hufford, and T. Manabe, 1991: A model for the complex permittivity of water at frequencies below 1 thz. *Int. J. Infrared Millimeter Waves*, **12**, 659–675.
- Locatelli, J. D., and P. V. Hobbs, 1974: Fall speeds and masses of solid precipitation particles. *J. Geophys. Res.*, **79**, 2185–2197.
- Matrosov, S., A. V. Korolev, and A. J. Heymsfield, 2002: Profiling cloud ice mass and particle characteristic size from doppler radar measurements. *J. Atmos. Ocean. Tech.*, **19**, 1003–1018.
- Matrosov, S., M. Shupe, A. J. Heymsfield, and P. Zuidema, 2003: Ice cloud optical thickness and extinction estimates from radar measurements. *J. Appl. Meteorol.*, **42**, 1584–1597.
- Miles, N. L., J. Verlinde, and E. E. Clothiaux, 2000: Cloud droplet size distributions in low-level stratiform clouds. *J. Atmos. Sci.*, **57**, 295–311.
- Mitchell, D. L., 2002: Effective diameter in radiation transfer: general definition, applications, and limitations. *J. Atmos. Sci.*, **59**, 2330–2346.
- Moran, K. P., B. E. Martner, M. J. Post, R. Kropfli, D. C. Welsh, and K. B. Widener, 1998: An unattended cloud-profiling radar for use in climate research. *Bull. Amer. Meteorol. Soc.*, **79**, 443–455.
- Morrison, H., J. A. Curry, V. I. Khvorostyanov, M. Shupe, and P. Zuidema, 2003: Development of a new double-moment microphysics parameterization: Application to Arctic stratiform clouds. p. manuscript in preparation.
- Parkinson, C. L., D. J. Cavalieri, P. Gloersen, H. J. Zwally, and J. C. Comiso, 1999: Arctic sea ice extents, areas, and trends, 1978–1996. *J. Geophys. Res.*, **104**, 20,837–20,856.
- Pavolonis, M. J., and J. R. Key, 2003: Antarctic cloud radiative forcing at the surface estimated from the AVHRR Polar Pathfinder and ISCCP D1 datasets, 1985–1993. *J. Appl. Meteorol.*, **42**, 827–840.
- Perovich, D. K., T. C. Grenfell, B. Light, and P. V. Hobbs, 2002: Seasonal evolution of the albedo of multiyear Arctic sea ice. *J. Geophys. Res.*, **107**, doi:10.1029/2000JC000,438.
- Persson, P. O. G., C. W. Fairall, E. L. Andreas, P. S. Guest, and D. K. Perovich, 2002: Measurements near the atmospheric surface flux group tower at SHEBA: Near-surface conditions and surface energy budget. *J. Geophys. Res.*, **107**, doi:10.1029/2000JC000,705.
- Pinto, J. O., 1998: Autumnal mixed-phase cloudy boundary layers in the Arctic. *J. Atmos. Sci.*, **55**, 2016–2038.
- Pinto, J. O., J. A. Curry, and J. M. Intrieri, 2001: Cloud-aerosol interactions during autumn over Beaufort Sea. *J. Geophys. Res.*, **106**, 15,077–15,097.
- Rangno, A., and P. Hobbs, 2001: Ice particles in stratiform clouds in the Arctic and possible mechanisms for the production of high ice concentrations. *J. Geophys. Res.*, **106**, 15,065–15,075.
- Rogers, D. C., P. J. DeMott, and S. M. Kreidenweis, 2001: Airborne measurements of tropospheric ice-nucleating aerosol particles in the Arctic spring. *J. Geophys. Res.*, **106**, 15,053–15,063.
- Rosenkranz, P. W., 1998: Water vapor microwave continuum absorption: A comparison of measurements and models. *Radio Sci.*, **33**, 919–928.
- Schweiger, A. J., and J. R. Key, 1994: Arctic Ocean radiative fluxes and cloud forcing estimates from the ISCCP C2 cloud dataset. *J. Appl. Met.*, **33**, 948–963.
- Selby, J., E. Shettle, and R. McClatchey, 1976: Atmospheric transmittance from 0.25 to 28.5 μm , Supplement LOW-TRAN 3B. *Air Force Geophys. Lab., Environ. Res. Pap.*, No. 587.
- Serreze, M., et al., 2000: Observational evidence of recent change in the northern high-latitude environment. *Clim. Change*, **46**, 159–207.
- Shupe, M. D., T. Uttal, S. Matrosov, and A. S. Frisch, 2001: Cloud water contents and hydrometeor sizes during the FIRE-Arctic Clouds Experiment. *J. Geophys. Res.*, **106**, 15,015–15,028.
- Stamnes, K., S. Tsay, W. Wiscombe, and I. Laszlo, 2000: A general-purpose numerically stable computer code for discrete-ordinate-method radiative transfer in scattering and emitting layered media. p. DISORT Report v1.1.
- Stankov, B. B., B. E. Martner, and M. K. Politovich, 1995: Moisture profiling of the cloudy winter atmosphere using combined remote sensors. *J. Atmos. Ocean. Tech.*, **12**, 488–510.
- Stone, R., 1997: Variations in western arctic temperatures in response to cloud radiative and synoptic-scale influences. *J. Geophys. Res.*, **102**, 21,769–21,776.
- Stone, R., J. Key, and E. Dutton, 1993: Properties and decay of stratospheric aerosols in the arctic following the 1991 eruptions of Mount Pinatubo. *Geophys. Res. Lett.*, **20**, 2359–2362.
- Stone, R., E. Dutton, J. Harris, and D. Longenecker, 2002: Earlier spring snowmelt in northern Alaska as an indicator of climate change. *J. Geophys. Res.*, **107**, doi:10.1029/2000JD000,286.
- Sturm, M., C. Racine, and K. Tape, 2001: Increasing shrub abundance in the Arctic. *Nature*, **411**, 546–547.
- Sun, Z., and K. Shine, 1994: Studies of the radiative properties of ice and mixed-phase clouds. *Q. J. R. Meteorol. Soc.*, **120**, 111–137.
- Turner, D., S. Ackerman, B. Baum, H. Revercomb, and P. Yang, 2003: Cloud phase determination using ground-based AERI observations at SHEBA. *J. Appl. Meteorol.*, **42**, 701–715.
- Uttal, T., and co authors, 2002: Surface heat budget of the Arctic ocean. *Bull. Amer. Meteorol. Soc.*, **83**, 255–275.

- Vavrus, S., 2003: The impact of cloud feedbacks on Arctic climate under greenhouse forcing. *J. Clim.*. Submitted.
- Walsh, J. E., and W. L. Chapman, 1998: Arctic cloud-radiation-temperature associations in observational data and atmospheric reanalyses. *J. Climate*, **15**, 1429–1446.
- Wang, S., Q. Wang, R. E. Jordan, and P. O. G. Persson, 2001: Interactions among longwave radiation of clouds, turbulence, and snow surface temperature in the Arctic: A model sensitivity study. *J. Geophys. Res.*, **106**, 15,323–15,333.
- Wang, X., and J. R. Key, 2003: Recent trends in Arctic surface, cloud, and radiation properties from space. *Sci.*, **299**, 1725–1728.
- Westwater, E. R., Y. Han, M. D. Shupe, and S. Y. Matrosov, 2001: Analysis of integrated cloud liquid and precipitable water vapor retrievals from microwave radiometers during the Surface Heat Budget of the Arctic Ocean project. *J. Geophys. Res.*, **106**, 32,019–32,030.
- Wood, R., C. Bretherton, and D. L. Hartmann, 2002: Diurnal cycle of liquid water path over the subtropical and tropical oceans. *Geophys. Res. Lett.*, **29**, doi:10.1029/2002GL015,371.
- Wylie, D., 2001: Arctic weather during FIRE/ACE 1998. *J. Geophys. Res.*, **106**, 15,363–15,375.
- Wylie, D., and J. Hudson, 2002: Effects of long-range transport and clouds on cloud condensation nuclei in the springtime Arctic. *J. Geophys. Res.*, **107**, doi:10.1029/2001JD000,759.
- Yum, S. S., and J. G. Hudson, 2001: Vertical distributions of cloud condensation nuclei spectra over the springtime Arctic Ocean. *J. Geophys. Res.*, **106**, 15,045–15,052.
- Zhang, T., K. Stamnes, and S. A. Bowling, 1996: Impact of clouds on surface radiative fluxes and snowmelt in the arctic and sub-arctic. *J. Clim.*, **9**, 2110–2123.
- Zuidema, P., and K. F. Evans, 1998: On the validity of the independent pixel approximation for boundary layer clouds observed during ASTEX. *J. Geophys. Res.*, **103**, 6059–6074.
- Zuidema, P., and D. Hartmann, 1995: Satellite determination of stratus cloud microphysical properties. *J. Climate*, **8**, 1638–1657.